Upslope Flows in Atmosphere and Water Tank, Part II: Fluid-Dynamical Smoothness as a Possible Cause for Velocity Similarity Violation

C. Reuten[*], S. E. Allen, and D. G. Steyn

Atmospheric Science Program, Department of Earth and Ocean Sciences, The University of British Columbia, Vancouver, Canada

Abstract: Water-tank models of meso-scale atmospheric processes often show good qualitative agreement of bulk quantities and flow characteristics and good quantitative agreement of turbulence quantities with field observations. However, it was demonstrated in the first part of this two-part communication that the similarity of velocities of thermally driven upslope flows in atmosphere and water tank is violated.

It is shown in this part that the velocities of thermally driven upslope flows in the atmosphere and in a water-tank model have statistically different dependences on proposed governing parameters. Of four substantially different hypotheses of upslope velocities, three agree with field observations because of large uncertainties and sparse data, but all hypotheses disagree with tank observations. One hypothesis that includes the influence of the total slope height agrees with field and tank observations when assuming fluid-dynamically rough atmospheric flows and fluid-dynamically smooth tank flows. The non-dimensional upslope flow velocities corresponding to rough and smooth flows depend differently on the governing parameters. Therefore, non-dimensional upslope flow velocities are different for atmosphere and water tank. Furthermore, as this hypothesis includes a dependence of the upslope flow velocity on the total height of the slope it implies that upslope flow systems are non-local phenomena.

Because fluid-dynamical roughness is technically difficult to achieve in water-tank models, velocity similarity violations can also be expected in water-tank models of other thermally driven meso-scale flows and our technique of explicitly including roughness length dependence may have wider applications.

Keywords: Bayesian analysis, physical scale model, scaling, similarity, upslope flows, water tank.

1. INTRODUCTION

Water-tank models have been used for several decades to study atmospheric phenomena. Some of the earlier experiments focused primarily on turbulence in the convective boundary layer (CBL) in salt- or heat-stratified water over a heated flat horizontal plate [1-6] and the role of turbulence in dispersion of pollutants [7-20]. Many of these studies investigated the CBL under externally imposed advection. Examples of thermally driven flows that have been studied with water-tank models are sea breezes [21], urban heat islands [22, 23] and their interactions [24], and upslope flows [25-27], which are the focus here. Simply speaking, upslope flows arise over heated sloping terrain in a stratified background fluid; fluid near the slope surface will be warmer than fluid at the same elevation further from the slope. Buoyancy and pressure-gradient forces together cause an upslope flow approximately parallel to the slope. This paper is the second part of a two-part communication. From here on we will refer to part I and part II for simplicity.

Previous tank studies of upslope flows showed similarity between atmosphere and water tank for turbulence parameters [28], flow characteristics [25, 29], and the order of magnitude of bulk quantities like CBL height and upslope flow velocity [26, 27]. In part I, it was shown that quantitative similarity can be achieved for CBL depth within approximately the uncertainty of field and tank observations (20%) but that upslope flow velocities are significantly different. Here in part II, the cause for the similarity violation of upslope flow velocity will be studied. A summary of the scaling and a description of the field and tank experiments are provided in section 2. In section 3, four alternative upslope flow velocity hypotheses are developed. In section 4 these are compared with field and tank observations using Bayesian analysis. A detailed discussion of the results is presented in section 5, and conclusions are drawn in section 6. The derivation of the equations used for the Bayesian analysis is provided in the appendix. Quantities in the atmosphere will be denoted with subscript 'a' to distinguish them from those in the water tank with subscript 'w'; no subscripts will be used if the quantity or equation applies to both atmosphere and water tank.

2. METHODS

a. Field Observations

Details of the field site and instrumentation at Minnekhada Park in the Lower Fraser Valley, British Columbia, Canada, are presented in [30]. The slope is fairly homogeneous over a width of roughly 3 km; the slope angle is approximately constant at 19° and ridge height is 760 m.

*Address correspondence to this author at the RWDI AIR Inc., Suite 1000, 736 8th Ave. SW, Calgary, AB T2P 1H4, Canada; Tel: 1-403-232-6771; Fax.: 1-403-232-6762; Email: creuten@gmail.com

Figure 2 in [30] suggests that a plateau better represents the terrain on the other side of the ridge than a slope. The plain adjacent to the slope is approximately flat. Observations used in this paper were taken under mostly cloudless skies in the morning hours of 25-26 July 2001, before the onset of sea-breeze and up-valley flows. Vertical profiles of moisture and temperature were measured with a tethersonde 3.5 km from the bottom of the slope. Early morning profiles showed roughly constant lapse rates up to about 1000 m, except very near the surface. Range-height indicator (RHI) scans with a lidar provided information on the backscatter boundary layer (BBL) depth over plain and slope, which reached values of about 800 m. Over the plain close to the slope a Doppler sodar was employed to measure vertical profiles of wind velocity averaged over approximately 20 minutes. 'Upslope flow velocities' were determined from each vertical profile as the maximum value of the horizontal component of the slope wind, typically 3-6 m s^{-1}.
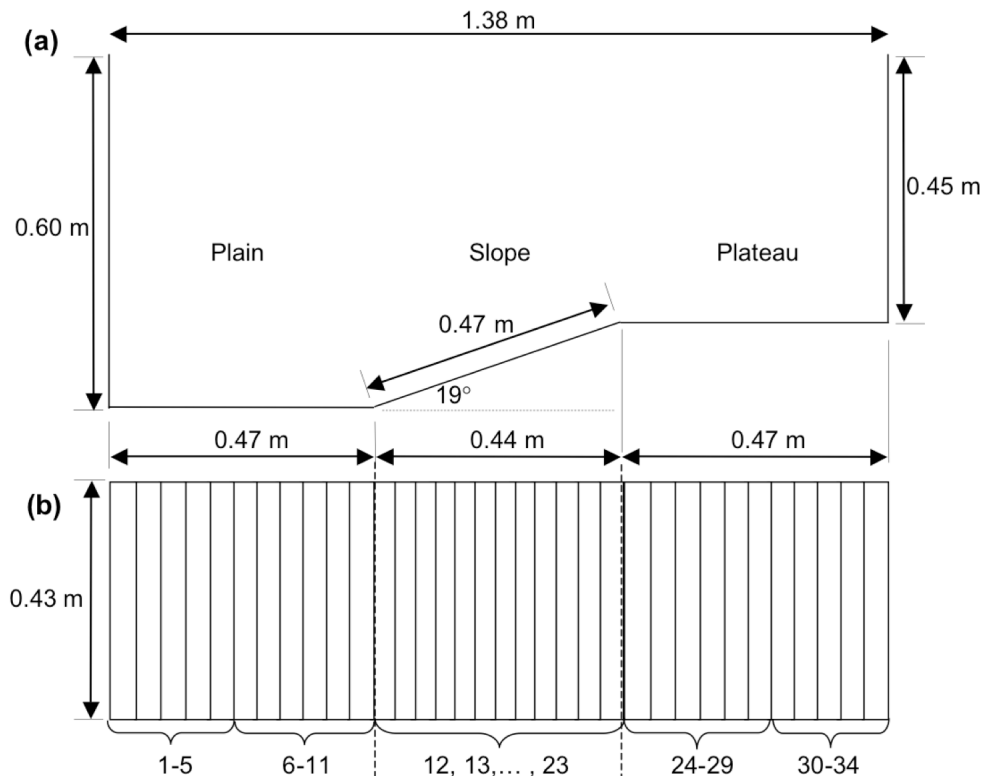
b. Water Tank

The water tank (Fig. **1**) has glass walls and a stainless steel bottom encased in a stainless steel frame. Because field observations showed fairly constant lapse rate all water-tank experiments were started with linear salt stratification. Convection is triggered in the tank by heating the bottom steel plate from below with strip heaters, which can be controlled individually or in groups of five to six heaters. Because heating could only be varied manually within 40-100% of the maximum power supply, all but one experiment were carried out with steady heat flux (Table **1**). In

experiment WT4, heat flux was manually controlled to approximate the roughly sinusoidal surface heat flux development found in the atmosphere. The experiments in Table **1** cover a wide range of parameter values and differ substantially in plain/plateau length and spatial and temporal variations of heat flux at the slope surface.

Two-dimensional velocity fields were measured from the motion of neutrally buoyant particles using the PIV ('particle image velocimetry') toolbox for Matlab®. Maximum upslope flow velocities were computed in two steps. First, medians over 20-s intervals were calculated to remove turbulent variations. Medians successfully removed outliers and were faster to calculate than means with outlier filters. Second, the medians of the maxima in three adjacent vertical profiles of horizontal velocities centered over the slope 20 cm upslope from its base were calculated to further smooth the data. The use of the median rather than the mean slightly reduced the influence of some extreme values. The results were very robust when averaging time was doubled and when five rather than three adjacent profiles were used. Experiments lasted roughly 1000 s. Maximum horizontal velocities ranged from 0.5-2.0 cm s^{-1}. More technical details can be found in [29].

c. Scaling

This section provides a summary of the scaling that was performed in part I of this paper. Mathematical idealizations were formulated for the atmosphere and the water tank and ten potentially relevant dimensional parameters were

Fig. (1). Schematic of the water tank. Scale is approximately 1:10. (**a**) Side view. (**b**) Plan view with strip heaters underneath the tank bottom numbered from 1 to 34. Heaters can be controlled individually underneath the slope and in two groups of five to six heaters each underneath plain and plateau as indicated.

Table 1. Overview of Water-Tank Experiments Used for Upslope Flow Velocities Analyses

Name	$N_w (\text{s}^{-1})$	$\overline{Q}_{H,w}$ (10^{-3} K m s^{-1})	$\Pi_{3,w}$	$L_{b,w}$ (m)	$L_{t,w}$ (m)	$Q_{H,w}$ Details (10^{-3} K m s^{-1})		
						Plain	Slope	Plateau
WT1	0.567	1.85	0.00117	0.470	0.470	1.85	1.85	1.85
WT2	0.379	1.85	0.00406	0.470	0.470	1.85	1.85	1.85
SP	0.379	1.85	0.00406	0.225	0.470	1.85	1.85	1.85
TR1	0.379	2.68	0.00588	0.470	0	1.48	1.67-3.70	-
TR2	0.342	3.15	0.00903	0.470	0	1.48/2.04	2.59-3.70	-
WT3	0.374	2.96	0.00649	0.470	0.470	1.85	2.96	1.85
WT4	0.423	1.48-3.52	0.00219-0.00521	0.470	0.470	1.48-3.52	1.48-3.52	1.48-3.52

Experiments are named according to their geometry as: WT ('Whole Tank'), SP ('Short Plain', additional end wall over the plain $L_{b,w} = 0.225$ m from the slope), and TR ('Triangular Ridge', additional end wall at the ridge top, $L_{t,w} = 0$); numbers distinguish experiments with equal geometry. $\Pi_{3,w}$ is computed for $\overline{Q}_{H,w}$, the surface heat flux spatially averaged over the slope only. The last three columns show details of the heat flux supplied to the tank. In TR1 the heat flux at the slope surface increased with height along the slope in twelve equal increments from 1.67 to 3.70×10^{-3} K m s^{-1}. In TR2, the slope surface heat flux increased from 2.39 to 3.70×10^{-3} K m s^{-1}, and the surface heat flux in left and right half of the plain was 1.48 and 2.04×10^{-3} K m s^{-1}, respectively. In WT4, heat flux was stepped up manually to roughly follow sinusoidal time development.

identified for the atmosphere and an additional two for the water tank: Ridge height H, sensible surface heat flux Q_H, buoyancy frequency N, horizontal length of slope L, total supplied energy density E, buoyancy parameter $g\beta$ (g is the gravitational acceleration and β the coefficient of thermal expansion), kinematic viscosity ν, thermal diffusivity κ, length of the plain L_b, length of the plateau L_t, and roughness height Z_r; in addition for the water tank its width W_w and the water depth over the plain D_w. We speculated in part I that the difference in Reynolds number, at the roughness height, may play an important role for the upslope flow velocity violation. In fluid-dynamically rough flow, the roughness elements lead to momentum roughness lengths much greater than thermal roughness lengths [31]. If the Reynolds number, at the scale of the roughness, is too small, molecular properties dominate and the appropriate momentum length and thermal length will be more similar. Thus, in part II, we change from using Z_r as a parameter, to introducing two separate parameters, the momentum z_m and thermal z_T roughness lengths. The Buckingham Pi Theorem [32] implies that the three involved fundamental units (K, m, s) require three independent key parameters, which were chosen to be H, Q_H, and N, to non-dimensionalize the remaining parameters and form nine atmospheric and eleven water-tank Pi Groups (Table **2**).

Convective boundary layer depth h is non-dimensionalized by dividing by H, $h^* = h/H$, and maximum upslope flow velocity U is non-dimensionalized by dividing by HN, $U^* = U/(HN)$. In the first part it was proposed that h^* and U^* only depend on the aspect ratio $\Pi_1 = L/H$, non-dimensional (ND) energy density $\Pi_2 = EN/Q_H$, and ND buoyancy parameter $\Pi_3 = g\beta Q_H/(H^2 N^3)$. Analyses of atmospheric and tank observations showed similarity of CBL

depth and a similarity violation of upslope flow velocity. The value of the aspect ratio Π_1 is the same for the idealized mathematical models of field site ('atmospheric idealization') and water-tank ('water-tank idealization') and can therefore not be responsible for the similarity violation. In this paper it will be investigated if the exponents m_1 and m_2 in the assumed monomial relationship $U^* = c\,\Pi_2^{m_1}\,\Pi_3^{m_2}$ are the same for atmospheric and tank observations. If they are the same then, because U^* differs, the coefficient c would have to be different and therefore depend not only on the aspect ratio Π_1 but also on other Pi groups, which are different for atmosphere and water tank. Before the functional dependence of U^* on Π_2 and Π_3 is further investigated, alternative hypotheses of upslope flow velocities are developed from the literature.

3. UPSLOPE FLOW VELOCITY HYPOTHESES

Four hypotheses of upslope flow velocities in atmosphere and water tank are proposed. Three are modifications of hypotheses extracted from the literature and for easy reference are named after the first author of the publications. To facilitate a comparison of the hypotheses, the notation is adapted to be the same across all hypotheses. The goal is to express the model predictions for ND upslope flow velocity in the form $U^* = c\,\Pi_2^{m_1}\,\Pi_3^{m_2}$. Further assumptions are necessary to bring the equations into this form. Most hypotheses include CBL depth h as a known external parameter. We treat h as an externally forced quantity and express it in terms of total supplied energy E. The assumption of an encroachment model [33] in part I led to similarity of CBL in atmosphere and water tank within expected uncertainties of 20%. The more realistic entrainment model [34] would only lead to improvements if further research could establish the dependence of the entrainment coefficient on the Pi groups Π_2 and Π_3. Heidt

Table 2.   **Summary of Pi Groups for Idealizations of the Atmosphere and the Water Tank. The Distinguishing Subscripts 'a' and 'w' were Dropped for Pi Groups that Apply to Both Idealizations**

Name	Symbol
Core Pi Groups	
Aspect ratio	$\Pi_1 = \dfrac{L}{H}$
ND energy density or time	$\Pi_2 = \dfrac{EN}{Q_H}$
ND buoyancy parameter / heat flux	$\Pi_3 = \dfrac{g\beta Q_H}{H^2 N^3}$
Molecular Pi Groups	
ND viscosity	$\Pi_4 = \dfrac{\nu}{H^2 N}$
ND thermal diffusivity	$\Pi_5 = \dfrac{\kappa}{H^2 N}$
Longitudinal Boundary Conditions	
ND half length of plain	$\Pi_6 = \dfrac{L_b}{H}$
ND half length of plateau	$\Pi_7 = \dfrac{L_t}{H}$
Water-Tank Specific Pi Groups	
ND tank width	$\Pi_{8,w} = \dfrac{W_w}{H_w}$
ND water depth	$\Pi_{9,w} = \dfrac{D_w}{H_w}$
Roughness Length Pi Groups	
ND momentum roughness length	$\Pi_{10} = \dfrac{z_m}{H}$
ND thermal roughness length	$\Pi_{11} = \dfrac{z_T}{H}$

[4] suggested a constant entrainment coefficient, but this is questioned by more recent research [35], and the additional shear caused by the upslope flow circulation further complicates the issue. For an encroachment model,

$$E_a = \frac{h_a \, \theta_{s,a}}{2} \text{ and } E_w = \frac{h_w \, \alpha_{s,w}}{2\alpha_{0,w}\beta_w} \,, \tag{1}$$

where $\theta_{s,a}$ is the potential temperature increase of the mean CBL potential temperature over the initial surface temperature and $\alpha_{s,w}$ is the specific volume increase of the mean CBL specific volume over the initial surface specific volume $\alpha_{0,w}$. Background stratifications in the encroachment model are

$$\gamma_a = \frac{\theta_{s,a}}{h_a} \text{ and } \gamma_w = \frac{\alpha_{s,w}}{\alpha_{0,w}\beta_w h_w} \,. \tag{2}$$

In both atmosphere and tank, these are related to the buoyancy frequencies by:

$$N = \left(g\beta\gamma\right)^{\frac{1}{2}} . \tag{3}$$

Substituting γ from (3) into (2), and the resulting equations for $\theta_{s,a}$ and $\alpha_{s,w}$ into (1), gives

$$h = \left(\frac{2g\beta E}{N^2}\right)^{\frac{1}{2}} \tag{4}$$

for atmosphere and water tank.

a. Hunt hypothesis

Hunt *et al.* [27] allowed for different dynamics in the surface, mixed, and inversion layers. They treated each layer separately and constrained parameters by smoothly matching adjacent layers at their common boundaries. They derived simplified forms of the Navier-Stokes equations for the different layers and matched unknown parameters at the interfaces. For the mean upslope flow velocity they derived

$$U_{M,a} \approx \Gamma_a \left(\sin\varphi \cdot g\beta_a h_a Q_{H,a}\right)^{\frac{1}{3}} . \tag{5}$$

Hunt *et al.* [27] assumed slope angles $\varphi \le 20°$, approximated $\sin\varphi \approx \varphi$, and estimated

$$\Gamma_a \sim \frac{1}{k}\ln\left(\frac{-L_{*,a}}{z_{m,a}}\right)\left[\frac{h_{s,a}}{h_a}\frac{1}{k}\ln\left(\frac{-L_{*,a}}{z_{T,a}}\right)\right]^{\frac{1}{3}} , \tag{6}$$

where ~ means 'is of same order of magnitude', $L_{*,a}$ is the Monin-Obukhov length, $h_{s,a}$ the surface layer depth, and $k \approx 0.4$ the von Kármán constant. Underlying (5) are the assumptions that

I.   CBL and upslope flow layer are identical;

II.   a deep unidirectional flow extends from the plain over the slope to the plateau without a return flow;

III.   the environmental stratification above the upslope flow layer is undisturbed;

IV.   the upslope flow velocity is independent of height within the mixed layer and is only slightly smaller than the maximum upslope flow velocity, which occurs in the surface layer; and

V.   Monin-Obukhov theory is valid over sloping terrain and Monin-Obukhov length and surface layer depth are independent of upslope flow characteristics.

The functional dependence of the coefficient Γ_a on its arguments in (6) and the values of the arguments are known only within order of magnitude. The dependence of Γ_a on momentum and thermal roughness lengths implies that ND maximum upslope flow velocity depends on Π_{10} and Π_{11} (Table **2**). This will be discussed further in section 5.

Initially, we will follow the suggestions in [27] that (5) also applies to upslope flows in water tanks and that $\Gamma \sim 10$ is roughly constant, therefore the dependence of U^* on Π_{10} and Π_{11} is negligible. Substituting (4) into (5) and using the definitions of the Pi groups in Table **2** gives

$$U_{Hunt}^* = \frac{U_{Hunt}}{HN} = c_{Hunt} \cdot \Pi_2^{1/6} \cdot \Pi_3^{1/2}, \tag{7}$$

where $c_{Hunt} = \Gamma \cdot 2^{1/6} \cdot (\sin\varphi)^{1/3}$.

b. Schumann Hypothesis

Schumann [36] ran a large-eddy simulation (LES) of the atmosphere above an unbounded, inclined, rough plane for constant and uniform heat flux and a linearly stratified background at rest. From the LES output Schumann determined the steady state maximum upslope flow velocities. Applying values typical of the Minnekhada site (slope angle of 19° and momentum roughness lengths ranging from 0.1 m to 1.0 m), Schumann's LES output gives

$$U_{\max,a} \approx 2.1 \left(g\beta_a \frac{Q_{H,a}}{N_a} \right)^{1/2}. \tag{8}$$

The field observations at Minnekhada Park never reached a steady state, as assumed in (8), before the onset of larger-scale flows roughly around noon contaminated slope flow observations. However, already at 1100 PST (Pacific Standard Time) on 25 July 2001 (from hereon called the 'test case', Table **4**), the observed maximum upslope flow velocity of 3.8 ± 0.5 m s^{-1} greatly exceeded the steady state value 1.5 m s^{-1} predicted by (8). Therefore, the 'Schumann hypothesis' is defined for atmosphere and water tank by replacing the empirical factor 2.1 in (8) with an unknown coefficient c_{Schu}, and using the definition of Π_3 in Table **2**:

$$U_{Schu}^* \equiv c_{Schu} \cdot \Pi_3^{1/2}. \tag{9}$$

c . Chen Hypothesis

Chen *et al.* [26] derived an upslope flow velocity scale for atmosphere and water tank from a balance between horizontal advection and pressure gradient term. Assuming again an encroachment model and using (4), a ND modification that allows for friction is given by,

$$U_{Chen}^* = c_{Chen} \cdot \Pi_2^{1/2} \cdot \Pi_3^{1/2}, \tag{10}$$

where $c_{Chen} = 1$ without friction. Further assumptions underlying (10) are:

(i) $h \leq H$;

(ii) CBL and upslope flow layer are identical;

(iii) CBL depth is equal over plain and slope;

(iv) the environmental stratification above the upslope flow layer is undisturbed; and

(v) the maximum upslope flow velocity occurs at the ridge top.

d. Gravity Current Hypothesis

Generalizing $U_{Chen} = U$ and $h = d$ in (10) and multiplying with H and N, gives

$$U = c_{Chen} (g_s d)^{1/2}, \tag{11}$$

where

$$g_s \equiv \begin{cases} g\beta_a \theta_{s,a} & \text{for atmosphere} \\ \dfrac{g}{\alpha_{0,w}} \alpha_{s,w} & \text{for water tank,} \end{cases} \tag{12}$$

is the reduced buoyancy scale; $\theta_{s,a}$, $\alpha_{s,w}$ and $\alpha_{0,w}$ as before. In the water tank, the upslope flow depth decreases over the slope towards the ridge height, and a plain-plateau flow at ridge height seems to act as a lid [29]. Thus, we suggest an alternative hypothesis,

$$U = c_{Grav} (g_s H)^{1/2}, \tag{13}$$

where H is the height of the ridge. It is interesting to note that this form of dependence is the same as for a gravity current flowing into a fluid of steadily decreasing depth at a given point, say the mid-point of the slope [37]. Of course, the geometry here is different as the current is actually on the slope. However, the variation in speed of a gravity current on a slope is a weak function of the slope [38] and will appear in a dependence on Π_1. Thus, we will refer to this hypothesis as the gravity current hypothesis. As above, applying an encroachment model giving (4) and using the definitions of the Pi groups in Table **2**, this alternative hypothesis can be defined for atmosphere and water tank by,

$$U_{Grav}^* = c_{Grav} \cdot \Pi_2^{1/4} \cdot \Pi_3^{1/4}. \tag{14}$$

Of all four hypotheses introduced in this section, only the gravity-current hypothesis gives a dimensional maximum upslope flow velocity that depends on the ridge height H, because Π_2 is independent of H and $\Pi_3^{1/2} \propto H^{-1}$, which cancels after multiplying (7), (9), and (10) by H and N. Therefore, only in the gravity-current hypothesis, the upslope flow velocity over any point of the slope depends on the height of the ridge that may be many kilometers (in the atmosphere) or tens of centimeters (in the tank) away and in that sense is the only one of the four hypothesis that treats upslope flows as non-local phenomena. The hypotheses are summarized in Table **3**.

4. RESULTS

In part I it was demonstrated that ND CBL depths in atmosphere and water tank were equal while ND upslope flow velocities were substantially different. The analysis was limited to particular points in time. Here the investigation will be much extended based on the four hypotheses introduced in the previous section.

If ND upslope flow velocities in atmosphere and water tank are functions of Π_1, Π_2, and Π_3, only, then the

hypotheses must hold for both systems. In particular, in a monomial of form

$$U^* = c \cdot \Pi_2^{m_1} \cdot \Pi_3^{m_2} \tag{15}$$

the constants m_1, m_2, and c must be equal for atmosphere and water tank. Note that the aspect ratio Π_1 is constant and equal in atmosphere and tank and therefore included in the constant c. Bayesian analysis is used to determine the joint probability density functions (PDF) of the exponents m_1 and m_2 given the data D. After marginalizing, i.e. integrating, over c (see Appendix)

$$p\left(m_1, m_2 \mid D\right) \propto \sum_{k=0}^{k_H}\left[\sum_{i=1}^{n}\left(U^*_i - c_L \cdot 10^{k/n_s} \cdot \Pi_{2,i}^{m_1} \cdot \Pi_{3,i}^{m_2}\right)^2\right]^{-n/2} , \tag{16}$$

where $k_H = n_s \log_{10}\left(c_H / c_L\right)$, n_s is the number of steps per order of magnitude in the range of c from a lowest value c_L to a highest value c_H, and n is the number of data points.

Table 3.   Summary of Hypotheses for ND Upslope Flow Velocities

Hypothesis	Equation
Hunt	$U_{Hunt}^* = c_{Hunt} \cdot \Pi_2^{1/6} \cdot \Pi_3^{1/2}$
Schumann	$U_{Schu}^* = c_{Schu} \cdot \Pi_3^{1/2}$
Chen	$U_{Chen}^* = c_{Chen} \cdot \Pi_2^{1/2} \cdot \Pi_3^{1/2}$
Gravity-current	$U_{Grav}^* = c_{Grav} \cdot \Pi_2^{1/4} \cdot \Pi_3^{1/4}$

In the mornings of 25 and 26 July 2001, $n = 23$ vertical profiles of wind speed were measured. For each profile i, the corresponding $\Pi_{2,i}$ and $\Pi_{3,i}$ were estimated and the ND maximum velocity U^*_i calculated. The contour plot of the PDF on the lhs of (16) is elliptic with a large ratio between major and minor axes and an almost 45° tilt relative to the Cartesian axes (Fig. **2a**). The reason for the strong tilt and ellipticity is a strong correlation between $\Pi_{2,a}$ and $\Pi_{3,a}$ (correlation coefficient 0.94), because both Pi groups depend on time t_a *via* $Q_{H,a}$ and E_a. It is possible to transform $\Pi_{2,a}$ and $\Pi_{3,a}$ into two approximately decoupled Pi groups $\Pi_{2,a}$ and $\Pi_{3,a}' = \Pi_{3,a}/\Pi_{2,a}$ (correlation coefficient -0.24), because $\Pi_{3,a}'$ only weakly depends on t_a for the morning hours used in the analysis [39]. Our field observations for the new Pi group $\Pi_{3,a}'$ cover only a narrow range from 2.5×10^{-5} to 4.1×10^{-5}. This narrow range is the main reason for the large uncertainty of the joint PDF $p\left(m_1, m_2 \mid D\right)$ in Fig. (**2a**) (large contour areas represent large uncertainty), besides measurement uncertainties and natural variability. To provide enough observational evidence for or against the various upslope flow velocity

hypotheses, a wide range of values for $\Pi_{3,a}'$ is needed. Because $\Pi_{3,a}'$ depends on maximum surface heat flux, stability, and only weakly on t_a, a wide range of $\Pi_{3,a}'$ requires observations to be carried out over several days with different background stabilities or at different times of year to achieve substantial differences in maximum surface heat flux.

The representation of $p\left(m_1, m_2 \mid D\right)$ in Fig. (**2a**) is more informative than individual confidence intervals of the exponents m_1 and m_2, which envelope the corresponding contour lines. For example, the 95% confidence intervals of m_1 and m_2 in Fig. (**2a**) include the Chen hypothesis, and based on these confidence intervals the Chen hypothesis cannot be rejected. However, because the Chen hypothesis lies outside of the 0.05 contour line, i.e. the 95% credible region, of the joint PDF of m_1 and m_2, the Chen hypothesis can be rejected. On the other hand, the Hunt, Schumann, and gravity-current hypotheses lie well within the 95% credible region and can therefore not be rejected by the field data.

Having greater control over the water-tank parameters and better and more measurements, results in a much narrower joint PDF for the water-tank (Fig. **2b**). Because heat flux was held steady in most tank experiments, $\Pi_{3,w}$ depends only weakly on time. Consequently, $\Pi_{2,w}$ and $\Pi_{3,w}$ are only weakly correlated and the ellipse in Fig. (**2b**) is only slightly stretched and tilted. A direct comparison of the joint PDF $p\left(m_1, m_2 \mid D\right)$ for atmosphere and water tank (Fig. **2a**) reveals that they are substantially different (with more than 95% probability). Hence, there is sufficient evidence in the field and tank data that ND upslope flow velocities have different functional relationships with Π_2 and Π_3. Moreover, all four hypotheses introduced in section 3 are far outside the 0.05 contour line of the tank PDF $p\left(m_1, m_2 \mid D\right)$. Because Π_1 is equal for atmosphere and tank and any dependence on Π_2 and Π_3 was already accounted for in (15), the coefficients c must depend on Pi groups other than Π_1, Π_2, and Π_3. In the following discussion section, evidence is provided for fluid-dynamically smooth tank flow. It will be determined how this leads to different functional dependence of U^* on Π_2 and Π_3 in the water tank. Possible dependencies on other Pi groups will be briefly discussed.

5. DISCUSSION

a. Dependence on Momentum Roughness Length

The Hunt hypothesis contains a very weak dependence of U^* on ND momentum roughness length Π_{10} through (6). Schumann [36] also found in his LES model runs a very weak dependence on ND momentum roughness length:

$$U_a^* \propto \Pi_{10,a}^{-0.033} \cdot \Pi_{3,a}^{1/2} \tag{17}$$
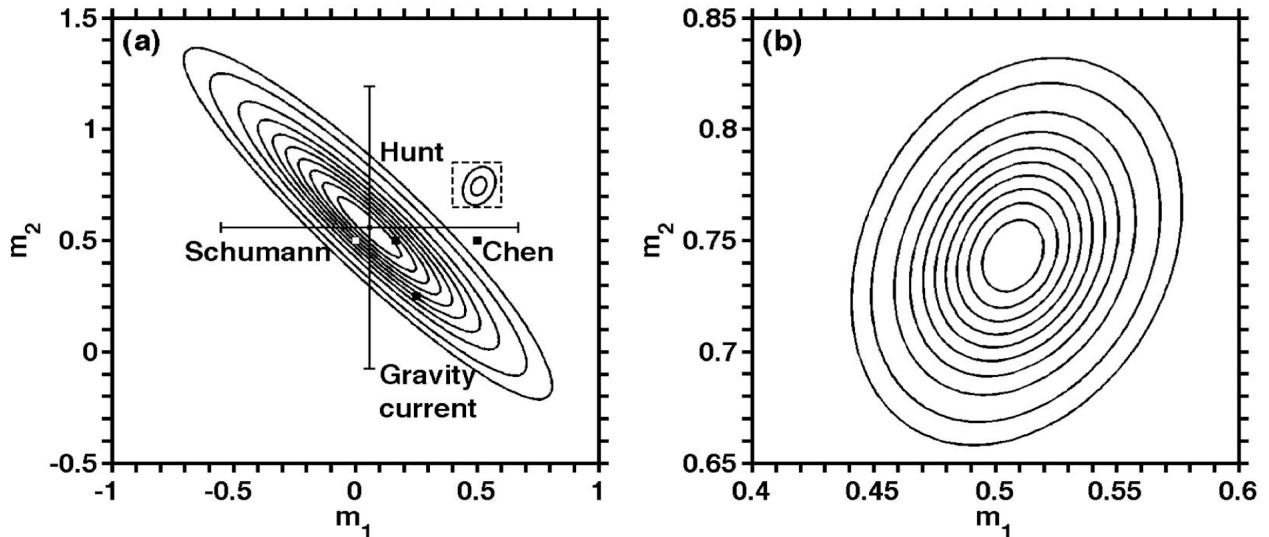
Fig. (2). Joint PDF $p(m_1, m_2 | D)$ of the exponents m_1 and m_2 in an empirical relationship $U^* = c \cdot \Pi_2^{m_1} \cdot \Pi_3^{m_2}$ between ND upslope flow velocity U^* and the two Pi groups Π_2 and Π_3. For the large ellipses in (**a**) and (**b**), contour lines are shown for 0.05 (outer line) and from 0.1 to 0.9 in steps of 0.1. (**a**) Large ellipse is for the field data on the mornings of 25 and 26 July 2001; small ellipse (only the 0.05 and 0.5 contour lines are shown) is for the data from seven water-tank experiments (Table **1**); labeled squares are the positions of the upslope flow velocity hypotheses discussed in section 3; error bars indicate 95% confidence intervals from a nonlinear regression. (**b**) Zoomed into the dashed region in (**a**) around the PDF for the tank data.

for a slope angle of 10°. Schumann's one-dimensional slope with the assumption of a steady state may not be a good representation of the field and water-tank observations used here, but it is worth pursuing the idea of a functional dependence of U^* on Π_{10} further. Assume a dependence on Π_{10} was contained in the coefficients c in the four hypotheses introduced in section 3. Separating this dependence from the coefficient generalizes (15):

$$U^* = c_1 \cdot \Pi_{10}^{-A} \cdot \Pi_2^{m_1} \cdot \Pi_3^{m_2}, \qquad (18)$$

where a minus sign was added to the exponent of Π_{10} because it can be expected that U^* is inversely related to Π_{10} so that the unknown parameter $A > 0$.

For the atmosphere, all but the Chen hypothesis give functional dependences of U^* on Π_2 and Π_3 that agree with field observations. Hence, the field observations support an approximately constant momentum roughness length in the atmosphere, as would be expected from land-use characteristics at the field site. For the water-tank observations, however, a hypothesis of form (18) requires that ND momentum roughness length $\Pi_{10,w}$ is a function of at least one of the two Pi groups $\Pi_{2,w}$ and $\Pi_{3,w}$. A hypothesis for such dependence will be presented next.

a. Similarity Violation as a Result of Fluid-Dynamic Feedback

In wind tunnel experiments, aerodynamical roughness is an important, yet often violated, scaling requirement [40]. In general, a flow is fluid-dynamically smooth if the viscous sublayer of depth

$$\delta_w \approx \frac{5\,v_w}{u_{*,w}} \qquad (19)$$

(chapter XX in [41]) is deeper than surface roughness protuberances. In the atmosphere over land surfaces, this is practically never the case [31]. However, an order-of-magnitude estimation shows that in our tank experiments the flow was fluid-dynamically smooth: The ratio between velocity and friction velocity is of order 10, i.e. $U_w / u_{*,w} \sim 10$ [41, 42]; with the tank values for U_w and v_w in Table **4** this gives $\delta_w \sim 0.01\,\mathrm{m}$, which is approximately two orders of magnitude larger than the roughness elements on the well-sanded and painted tank bottom.

Because of fluid-dynamical smoothness, momentum roughness length in the water tank is not a function of distribution and size of roughness elements but of viscosity and friction velocity (Chapter 7 in [42]):

$$z_{m,w} \approx \frac{0.11\,v_w}{u_{*,w}}. \qquad (20)$$

An increase of upslope flow velocity leads to increased friction velocity, which in turn leads to decreased roughness length in (20). This permits further increase of upslope flow velocity. A possible approach to quantifying this positive fluid-dynamical feedback will be presented next.

b. Quantification of Fluid-Dynamic Feedback

The goal is to express U_w^* as a monomial of the two Pi groups $\Pi_{2,w}$ and $\Pi_{3,w}$ by substituting (20) into the definition of $\Pi_{10,w}$ in Table **4**, which is substituted into (18) to give

$$U_w* \approx c_1 \cdot \left(\frac{0.11 \nu_w}{u_{*,w} H_w} \right)^{-A} \cdot \Pi_2^{m_1} \cdot \Pi_3^{m_2} \qquad (21)$$

To express the friction velocity $u_{*,w}$ in terms of known quantities, we use convective transport theory [43],

$$u_* = \left(C_{*D} w_* U \right)^{1/2}, \qquad (22)$$

where the momentum transport coefficient C_{*D} depends on the surface characteristics, U is the maximum in the vertical profile of upslope flow velocity, and

$$w_* = \left(g\beta h Q_H \right)^{1/3} \qquad (23)$$

is the convective velocity scale.

Table 4.   Data for Test Case

Name	Symbol (Units)	Atmosphere	Water Tank
Ridge height	H (m)	760	0.149
Instantaneous heat flux	Q_H (K m s^{-1})	0.21 ± 0.05	$(1.9 \pm 0.2) \times 10^{-3}$
Energy density	E (K m)	1600 ± 400	0.56 ± 0.05
Buoyancy frequency	N (s^{-1})	0.015 ± 0.001	0.38 ± 0.02
Buoyancy parameter	$g\beta$ (m s^{-2} K^{-1})	0.036	0.0026
Kinematic viscosity	ν (m^2 s^{-1})	1.52×10^{-5}	8.9×10^{-7}
Prandtl number at 25°C	Pr	0.72	6.1
CBL depth	h (m)	720 ± 120	0.14 ± 0.02
Upslope flow velocity	U (m s^{-1})	3.8 ± 0.5	0.005 ± 0.001

Atmospheric data are for the field site at Minnekhada Park at 1100 PDT 25 July 2001; water-tank experiment was designed such that, i.e. $\Pi_{2,w} = \Pi_{2,a}$ and $\Pi_{3,w} = \Pi_{3,a}$. Uncertainties roughly represent 95% confidence intervals.

Equation (22) was extensively validated for atmospheric convection over land and ocean surfaces [43-45]. The derivation of (22) in [43] applies equally to free convection in air or water. It assumes that surface- and micro-layer processes can be ignored, therefore it can also be applied to fluid-dynamically smooth flow. To ignore these processes, they must be fast enough to maintain higher temperatures in surface- and micro-layer than in the mixed layer. This was the case in all tank experiments, because convection and upslope flows continued for at least another minute after heat flux was shut down. Stull [43] showed that (22) also holds under non-calm conditions as long as the mixed-layer Richardson number

$$R_* \equiv \left(\frac{w_B}{U} \right)^2, \qquad (24)$$

is greater than 3 ('quasi-free convection'). Here, the buoyancy velocity scale w_B is defined by

$$w_B^2 \equiv \begin{cases} g\beta_a \Delta\theta_{skin,a} h_a & \text{for atmosphere} \\ \dfrac{g}{\alpha_{0,w}} \Delta\alpha_{skin,w} h_w & \text{for water tank,} \end{cases} \qquad (25)$$

where $\Delta\theta_{skin,a}$ and $\Delta\alpha_{skin,w}$ are the differences of potential temperature at the land surface and specific volume at the tank bottom to the corresponding quantities in the mixed layer. All other quantities were introduced before, and typical values used here are given in Table **4**. Because we do not have measurements of the skin temperatures, we estimate lower limits. At the field site we measured differences between 2-m and mixed-layer temperatures of approximately 2 K. Because skin temperatures can be expected to be substantially larger, we use $\Delta\theta_{skin,a} = 3\,\text{K}$ as a lower limit, which was also the lowest value observed in Oklahoma under much weaker surface heat fluxes [43]. Substituting this value into (25) gives $w_{B,a} > 9\,\text{m s}^{-1}$, and the mixed-layer Richardson number becomes $R_{*,a} > 5$, meeting the requirement for quasi-free convection. In the water tank, rising thermals hitting the CT probes lead to rapid increases in specific volume, which are used here as a conservatively low estimate of the difference between skin and mixed-layer temperatures: $\Delta\alpha_{skin,w} = 0.5 \times 10^{-6}\,\text{m}^3\,\text{kg}^{-1}$ (Fig. **7** in [29]). This value gives $w_{B,w} > 0.02\,\text{m s}^{-1}$ and $R_{*,w} > 16$, indicative of quasi-free convection.

The convective boundary-layer depth h is substituted from the encroachment model (4) to give the convective velocity scale (23). Then the convective velocity scale (23) is substituted into (22) to give the friction velocity, which is substituted into (21) to give

$$U_w* \approx c_1 \cdot \left\{ \frac{0.11 \nu_w}{\left[C_{*D,w} \left(g\beta_w \left(\frac{2g\beta E}{N^2} \right)^{1/2} Q_{H,w} \right)^{1/3} U_w \right]^{1/2} H_w} \right\}^{-A} \cdot \Pi_{2,w}^{m_1} \cdot \Pi_{3,w}^{m_2}. \quad (26)$$

On the rhs of the last equation, the viscosity ν_w appears, so that ND upslope flow velocity depends on ND viscosity $\Pi_{4,w}$. Moreover, the appearance of upslope flow velocity U_w with the positive exponent $A/2$ on the rhs quantifies the positive feedback mechanism described qualitatively in the previous subsection. Expanding the rhs with monomials of H_w and N_w, applying the definitions of $\Pi_{2,w}$, $\Pi_{3,w}$, and $\Pi_{4,w}$ in Table **2**, and solving for U_w* yields

$$U_w* \approx c_1^{\frac{2}{2-A}} \cdot 0.11^{\frac{-2A}{2-A}} \cdot 2^{\frac{A}{6(2-A)}} \cdot C_{*D,w}^{\frac{A}{2-A}} \cdot \Pi_{4,w}^{\frac{-2A}{2-A}} \cdot \Pi_{2,w}^{\frac{A+12m_1}{6(2-A)}} \cdot \Pi_{3,w}^{\frac{A+4m_2}{2(2-A)}}. \quad (27)$$

The first three factors are constant. The fourth and fifth factors are not constant, but the tight contour lines in Fig. (**2**) suggest that they did not vary much. This will be further

discussed below. The pairs of exponents $\left(\dfrac{A+12m_1}{6(2-A)}, \dfrac{A+4m_2}{2(2-A)} \right)$ are a parametric representation of a path in the $m_1 \times m_2$ plane. Each point on the path corresponds to a particular value of the exponent A of ND momentum roughness length $\Pi_{10,w}$ in (18). Most probable values of A are those within the PDF contours near the mode of $p(m_1, m_2 | D)$. There are four different paths, one for each hypothesis introduced in section 3 and its fixed pair (m_1, m_2) of exponents (Fig. **3a**). Only the path for the gravity-current hypothesis is within the 5% contour of the PDF and runs close to the mode (Fig. **3b**). There is a range of probable values for A. Representative values of simple rationals for A are shown in Fig. (**3b**). We chose for the following discussion $A = 3/4$ fairly close to the mode, because it seems more likely that this value could be derived from first principles than 4/5 or 5/6. The gravity-current hypothesis therefore agrees well with water-tank observations if the ND momentum roughness length with an exponent of $A = 3/4$ is included in (27):

$$U_w^* \approx 15.15 \; c_1^{8/5} \cdot C_{*D,w}^{3/5} \cdot \Pi_{4,w}^{-6/5} \cdot \Pi_{2,w}^{1/2} \cdot \Pi_{3,w}^{7/10} = c_{2,w} \cdot \Pi_{2,w}^{1/2} \cdot \Pi_{3,w}^{7/10} . \quad (28)$$

Substituting $A = 3/4$ into (18) gives the corresponding equation for the atmosphere:

$$U_a^* = c_1 \cdot \Pi_{10,a}^{-3/4} \cdot \Pi_{2,a}^{1/4} \cdot \Pi_{3,a}^{1/4} = c_{2,a} \cdot \Pi_{2,a}^{1/4} \cdot \Pi_{3,a}^{1/4} . \quad (29)$$

Here $c_{2,a}$ depends on surface characteristics and slope angle, but is constant with respect to the quantities changed

in our experiments listed in Table **1**: N_w, $Q_{H,w}$, and E_w. In the water tank, $c_{2,w}$ depends rather strongly on N_w: $c_{2,w} \propto N_w^{6/5}$. However, because $U_w^* \propto N_w^{-2/5} \cdot E_w^{1/2} \cdot Q_{H,w}^{1/5}$ and the range of buoyancy frequency N_w and instantaneous heat flux $Q_{H,w}$ in our tank experiments is rather small (Table **1**), the posterior distribution of U_w^* in Figs. (2, 3) is dominated by E_w, which ranges from 0 to its maximum value. More experiments over a much wider range of buoyancy frequencies N_w will be required in the future to test the dependence of ND upslope flow velocity on N_w and therefore test the applicability of convective transport theory to upslope flows in water tanks.

c. Plausibility Test and Future Research Needs

From the data of the test case in Table **4**, $U_a^* = 0.33$ and $U_w^* = 0.088$. It seems counterintuitive at first that a fluid-dynamically smooth flow is slower than a rough flow. Estimating roughly $z_{m,a} \approx 0.3$ m at the field site, the momentum roughness length in the tank that is required from similarity with the atmosphere, $\Pi_{10,w} = \Pi_{10,a}$, is $z_{m,w} = z_{m,a} H_w / H_a \approx 0.06$ mm. In other words, if the flow in the tank was fluid-dynamically rough with a roughness length of 0.06 mm then similarity of ND upslope flow velocity could be expected. However, the smooth flow in the tank has the characteristics of a rough flow over a surface with much larger momentum roughness length: Field observations for the test case (Table **4**) substituted into (29)
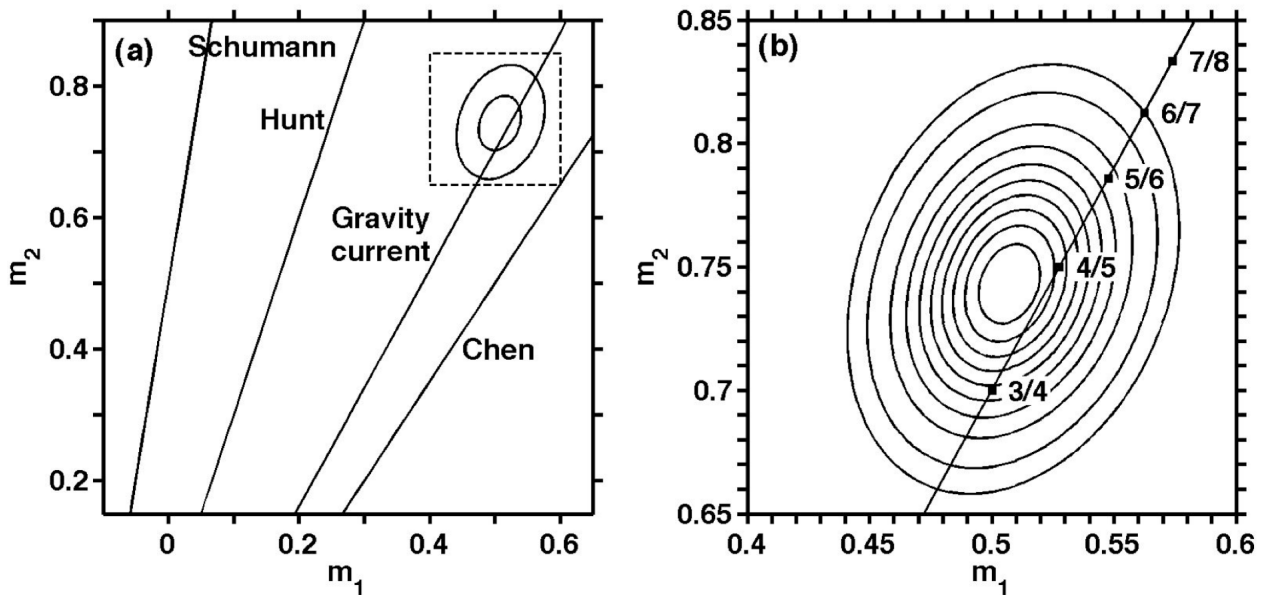

Fig. (3). Parameter paths of the exponent A in upslope flow velocity hypotheses of form $U_w^* = c_1 \cdot \Pi_{10,w}^{-A} \cdot \Pi_{2,w}^{m_1} \cdot \Pi_{3,w}^{m_2}$, superimposed on the joint PDF of m_1 and m_2 for the tank observations, only. The pairs $\left(\dfrac{A+12m_1}{6(2-A)}, \dfrac{A+4m_2}{2(2-A)} \right)$ are shown for four upslope flow velocity hypotheses as labeled in (**a**). Contour plots of the PDF are shown as in Fig (**2**). (**b**) is zoomed into the dotted rectangular region of (**a**). Representative values of A are shown in (**b**) as labeled squares.

give $c_1 \approx 1.1 \times 10^{-3}$. A corresponding rough flow in the water tank should follow the equivalent equation to (29),

$$U_w* = c_1 \cdot \Pi_{10,w}^{-3/4} \cdot \Pi_{2,w}^{1/4} \cdot \Pi_{3,w}^{1/4}, \qquad (30)$$

with the same value for c_1 as in the atmosphere. Substituting this value and the tank observations of the test case (Table **4**) into (30) gives $z_{m,w} \approx 0.3$ mm . In other words, with respect to momentum roughness length, the smooth flow in the water tank represents a rough atmospheric flow over a surface with a roughness length about five times greater than the one estimated for the field site. Therefore, from (29), the ND upslope flow velocity in the atmosphere should be $5^{3/4}$ times the tank value, in good agreement with the data above.

The dependence of the gravity-current hypothesis on roughness length as detailed here can only be tentative and guide in a search for underlying first principles. Future research will have to address several questions and challenges: Is convective transport theory applicable to smooth flows? Can the unknown coefficients c_1 and $C_{*D,w}$ in (28) be derived from first principles? Moreover, it is desirable to refine the upslope flow velocity hypotheses by replacing the encroachment model with the entrainment model. Finally, with more tank data the probability density function of m_3 in an upslope flow hypothesis of form

$$U_w = c_w \cdot \Pi_{4,w}^{m_3} \cdot \Pi_{2,w}^{m_1} \cdot \Pi_{3,w}^{m_2} \qquad (31)$$

can be determined and compared with $m_3 = -6/5$ in (28).

Such future research would make it possible to quantitatively scale between water tank and atmosphere, albeit not simply by applying (15) with the constants m_1, m_2, and c being equal for atmosphere and water tank. Currently, even if fluid-dynamical smoothness could be overcome in water-tank experiments, the constants m_1, m_2, and c in (15) remain poorly constrained. Particularly, more accurate field data for nearly idealized environmental settings are needed. This paper suggests that previously observed quantitative agreement was within the uncertainties associated with field and tank measurements and with environmental settings that were either badly known or difficult to model in the water tank. However, previous research mentioned in the introduction has demonstrated the value of water-tank experiments to qualitatively model atmospheric flows over sloping terrain. For example, Reuten *et al*. (2007) demonstrated similar development of pollutant layers in water tank and field observations.

d. The Role of Other Pi Groups

The previous subsections of the discussion provide a tentative explanation for the different functional dependences of ND upslope flow velocities in tank and atmosphere on the governing parameters. The explanation focused on the importance of momentum roughness length Π_{10} in the atmosphere and led to the inclusion of ND viscosity Π_4 in the water tank. A brief discussion of the

potential role of other ND governing parameters is provided next.

Thermal Roughness Length and Diffusivity

A hint at another important difference between tank and atmosphere comes from [27], who included the thermal roughness length z_T, (5) and (6). The ratio between momentum and thermal roughness length strongly depends on the Prandtl number (which is very different for air and water, Table **4**) and surface properties. For the field site, $z_{m,a} \gg z_{T,a}$ [31], and for smooth tank flow $z_{m,w} \gg z_{T,w}$ by many orders of magnitude (table 4.1 in [46]). Hence, heat transport is very inefficient in both systems. Further research into the coefficient Γ_a for the atmosphere in [27], (6), and Γ_w for the water tank is required to assess the impact of a similarity violation of ND thermal roughness length $\Pi_{11} = z_T / H$ on upslope flow velocity in the Hunt hypothesis. It was shown above that the characteristics of fluid-dynamically smooth flow introduce a dependence on ND viscosity $\Pi_{4,w}$ in (28). Future research will have to investigate if a dependence of ND upslope flow velocity on ND thermal roughness length Π_{11} introduces a dependence on ND thermal diffusivity $\Pi_{5,w}$ in the water tank.

Reynolds Number

As the flow is dependent on the viscosity, it is Reynolds-number (Re) dependent. A more direct and usual route would be to investigate the effect of Reynolds number directly, rather than consider roughness lengths. However, as was pointed out in part I, this approach is inconclusive. The critical Reynolds number, above which the flow would be dominated by turbulence, is strongly dependent on the choice of length and velocity scales and the particular system and flow geometry. Using the definition in [26], the tank experiments used in this part give $Re = LU/\nu = (2.2 - 8.7) \times 10^3$. According to [26], this would suggest similarity with the atmosphere based on a critical pipe flow Reynolds number. However, the geometry in the water tank is not that of a pipe flow and may therefore have a different critical value. An example of a different geometry (a plume stack) is given by Contini *et al*. (2009) where they find that a value of 2196 in a wind tunnel is insufficient to achieve similarity with the full-scale atmosphere. In contrast [39] defined the Reynolds number based on upslope-flow profiles observed in the tank assuming the geometry of an open channel flow: Only for the fastest flows observed in our experiments, values in the range 1350-1800 of intermittently turbulent flow are reached. The approach taken in this study *via* the momentum roughness lengths provides deeper insight into the flow characteristics in the tank.

Plain and Plateau Lengths

Non-dimensional plain and plateau lengths, $\Pi_{6,w}$ and $\Pi_{7,w}$, cannot be significant for the similarity violation. The water-tank experiments (Table **1**) had substantially different

$\Pi_{6,w}$ and $\Pi_{7,w}$ but $p(m_1, m_2|D)$ is very narrow. Furthermore, $p(m_1, m_2|D)$ for all seven experiments is narrower than for any subset of six experiments (not shown). In other words, each tank experiment contributes to improved predictions of m_1 and m_2 even if inclusion of the data increases the range of $\Pi_{6,w}$ and $\Pi_{7,w}$.

Tank Width

Observations early into the tank experiments show no influence of friction at the lateral side walls of the tank on upslope flow velocities near the slope centre. At later times, which we did not use for the analyses here, more complex 3D flow structures developed which can be attributed to temperature gradients and possibly friction at the lateral side walls (figure 8 in [29]). The opposite effect, lateral side walls suppressing horizontally mass-compensating flows and forcing return flows against gravity above the upslope flow, seems plausible. However, despite a lack of lateral confinement at the field site [30] observed flows in downslope direction above the upslope flows, which compensated most of the upslope mass flux. Therefore, ND upslope flow velocities should not substantially depend on ND tank width $\Pi_{8,w}$.

Water Depth and Gravity Waves

Non-dimensional water depth over the plain, $\Pi_{9,w}$, is unlikely an important factor for upslope flow velocities, because in all experiments the water surface was far above the top of the CBL. In agreement with [25], we observed elevated layers of alternating flows above the plain-plateau flow. These were shallow, their velocities decreased substantially with height, and they never seemed to affect water near the top surface.

An indirect effect of the confinement of the tank by $\Pi_{6,w}$ to $\Pi_{9,w}$ could be that energy dissipation by gravity waves in the atmosphere is greater than in the water tank, but that contradicts observations of greater upslope flow velocities in the atmosphere (part I). In can be concluded that it is unlikely that ND upslope flow velocities depend substantially on $\Pi_{6,w}$ to $\Pi_{9,w}$ and that such a dependence could explain the similarity violation.

CONCLUSIONS

Four hypotheses for ND maximum upslope flow velocities were introduced based on [27, 36, 26], and a gravity-current flow into a fluid of decreasing depth. The hypotheses were all of form $U^* = c \cdot \Pi_2^{m_1} \cdot \Pi_3^{m_2}$ with unknown coefficient c. $\Pi_2 = \dfrac{EN}{Q_H}$ and $\Pi_3 = \dfrac{g\beta Q_H}{H^2 N^3}$ were initially assumed the only governing ND parameters. The Bayesian joint PDF of the exponents m_1 and m_2 differed between atmosphere and water tank with greater than 95% probability. The Hunt, Schumann, and gravity-current hypotheses agreed well with the PDF for the field data, but none of them agreed with the PDF for the tank data. It was concluded that ND upslope flow velocity requires additional dependence on other Pi groups. Observational evidence rules out Pi groups related to the size and geometry of the tank ($\Pi_{6,w}$ to $\Pi_{9,w}$). Estimations of surface roughness and viscous sublayer depth suggest that the upslope flow in the water tank is fluid-dynamically smooth, and therefore momentum roughness length $z_{m,w}$ depends on friction velocity. This results in a stronger dependence of U_w^* on $\Pi_{2,w}$ and $\Pi_{3,w}$ in the tank than in the atmosphere, because an increase of $\Pi_{2,w}$ or $\Pi_{3,w}$ leads to a decrease of $z_{m,w}$ and therefore stronger increase of U_w^* than for fluid-dynamically rough flow. It was demonstrated that only for the gravity-current hypothesis the inclusion of ND momentum roughness length in U_w^* can lead to good agreement with the tank data. This success of the gravity-current hypothesis suggests that upslope flows must be treated as non-local phenomena, because only in the gravity-current hypothesis are upslope flow velocities dependent on ridge height.

More research should be carried out to test the applicability of convective transport theory to smooth flows, to replace the encroachment model of CBL growth by the more realistic entrainment model, and to test the predicted value -6/5 of the exponent of ND viscosity $\Pi_{4,w}$ in (28).

The work presented here implies that water-tank models of other thermally driven meso-scale circulations like up-valley flows, sea breezes, and urban heat islands may suffer the same velocity similarity violation as upslope systems. It is difficult in a laboratory setting to ensure both fluid-dynamically rough flow and a match between roughness elements in the atmosphere and tank. However, as shown here, it is possible to explicitly include the dependence on the momentum roughness length and use the tank data to distinguish between flow dependence models for the atmosphere.

ACKNOWLEDGEMENTS

APPENDIX

Bayesian Parameter Estimation

This appendix briefly derives the equations used in this communication. Background information and details of the following derivations can be found in [47-50].

Starting point is Bayes' Theorem

$$p(\theta|D,I) = \frac{p(\theta|I)\,p(D|\theta,I)}{p(D|I)}\,. \tag{1}$$

Here, the arguments are propositions and p denotes probabilities of their truths. We follow the common practice to drop the terminology involving 'proposition'; instead we interpret $p(\theta|D,I)$ as the joint probability density function (PDF) of the (unknown) model parameters m_1, m_2, and c in (15) and their standard deviation σ, given the n data $d_1,...,d_n$ and the background information I. Note that σ is dominated by unknown environmental noise and therefore must be modeled as an unknown parameter. On the rhs, $p(\theta|I)$ is the 'prior probability' assigned to m_1, m_2, c, and σ before knowledge of the data; $p(D|\theta,I)$ is the 'likelihood' of the data, which is the sampling distribution of the data given particular parameter values m_1, m_2, c, and σ; finally, the 'global likelihood' $p(D|I)$ is a normalization constant. Each of the factors in (1) contains a conditional dependence on the background information I, which will be dropped for the remainder of this appendix. Thus, Bayes' theorem (1) becomes

$$p(m_1,m_2,c,\sigma|D) \propto p(m_1,m_2,c,\sigma)\,p(D|m_1,m_2,c,\sigma). \tag{2}$$

The likelihood on the rhs is treated first. From the background information, the individual observations can be expressed as

$$d_i = f_i + e_i, \tag{3}$$

where f_i is the model's prediction of the ith datum; the e_i follow a normal distribution with mean zero and standard deviation σ. Let D_i denote the proposition that the ith datum is d_i, so that $D = D_1,...,D_n$. Similarly, define propositions on the errors, such that $E = E_1,...,E_n$. The sampling distribution of the noise is Gaussian,

$$p(E_i|\sigma) = \frac{1}{\sqrt{2\pi}\,\sigma}\exp\left(-\frac{e_i^2}{2\sigma^2}\right). \tag{4}$$

Substituting e_i from (3) gives the sampling distribution of the data

$$p(D_i|\theta) = \frac{1}{\sqrt{2\pi}\,\sigma}\exp\left[-\frac{(d_i - f_i)^2}{2\sigma^2}\right], \tag{5}$$

which depends on all parameters θ and σ and the background information I. Because the individual observations are independent of each other and the noise is independent and identically distributed, the product rule of probability theory implies,

$$p(D_1,...,D_n|\theta) = \prod_{i=1}^{n} p(D_i|\theta). \tag{6}$$

Substituting (5) into (6) gives

$$p(D|\theta,\sigma) = \frac{1}{(2\pi)^{n/2}\sigma^n}\exp\left[-\frac{1}{2\sigma^2}\sum_{i=1}^{n}(d_i - f_i)^2\right]. \tag{7}$$

Applied to the data and hypotheses in this paper the last equation becomes

$$p(D|m_1,m_2,c,\sigma) = \frac{1}{(2\pi)^{n/2}\sigma^n}\exp\left[-\frac{1}{2\sigma^2}\sum_{i=1}^{n}\left(U^*_i - c\cdot\Pi_{2,i}^{m_1}\cdot\Pi_{3,i}^{m_2}\right)^2\right], \tag{8}$$

where U^*_i are the non-dimensionalized observed upslope flow velocities, $f_i = c\cdot\Pi_{2,i}^{m_1}\cdot\Pi_{3,i}^{m_2}$ is the model function evaluated at the values of Π_2 and Π_3 corresponding to each observation i, and m_1, m_2, and c are the model parameters.

The first factor on the rhs in (2), the prior probability, can be split using the product rule and assuming that all four parameters m_1, m_2, c, and σ are *a priori* independent of each other,

$$p(m_1,m_2,c,\sigma) = p(m_1)\,p(m_2)\,p(c)\,p(\sigma). \tag{9}$$

The intention here is to be maximally non-committal about the parameters m_1, m_2, c, and σ within sufficiently wide lower and upper boundaries. This can be achieved in two fundamentally different ways [50]. 'Location' parameters can be either positive or negative and usually have a relatively narrow prior range, which applies to m_1 and m_2. They are assigned uniform priors

$$p(m_1) = \frac{1}{m_{1,H} - m_{1,L}} \quad\text{and}\quad p(m_2) = \frac{1}{m_{2,H} - m_{2,L}}, \tag{10}$$

where the subscripts L and H denote lower and upper boundaries, respectively. By contrast, 'scale parameters' are always positive and the lower and upper boundaries often span several orders of magnitude. The standard deviation σ and the constant factor c are both treated as scale parameters, which are assigned Jeffreys priors:

$$p(\sigma) = \frac{1}{\sigma\ln(\sigma_H/\sigma_L)} \quad\text{and}\quad p(c) = \frac{1}{c\ln(c_H/c_L)}. \tag{11}$$

Now the rhs of (2) can be determined, but the quantity of interest is $p(m_1,m_2|D)$, which can be determined from $p(m_1,m_2,c,\sigma|D)$ by 'marginalizing' over the two parameters c and σ:

$$p(m_1,m_2|D) = \int_{\sigma_L}^{\sigma_H}\int_{c_L}^{c_H} p(m_1,m_2,c,\sigma|D)\,dc\,d\sigma. \tag{12}$$

Substituting (2) and (8)-(11) into (12) gives

$$p(m_1,m_2|D) \propto \int_{c_L}^{c_H}\frac{1}{c}\int_{\sigma_L}^{\sigma_H}\frac{1}{\sigma^{n+1}}\exp\left[-\frac{1}{2\sigma^2}\sum_{i=1}^{n}\left(U^*_i - c\cdot\Pi_{2,i}^{m_1}\cdot\Pi_{3,i}^{m_2}\right)^2\right]d\sigma\,dc. \tag{13}$$

Following the derivation leading to (C.17) in [50] and assuming that the boundaries of integration over σ are so

wide that practically $\sigma_L \to 0$ and $\sigma_H \to \infty$, the inner integral of (13) simplifies so that,

$$p\left(m_1, m_2 \mid D\right) \propto \int_{c_L}^{c_H} dc \frac{1}{c} \left[\sum_{i=1}^{n} \left(U^*_i - c \cdot \Pi_{2,i}^{m_1} \cdot \Pi_{3,i}^{m_2}\right)^2 \right]^{-n/2}, \quad (14)$$

where the gamma function that results from the integration is absorbed in the proportionality.

The integral in (14) is replaced by a sum in which both c_k and the step length Δc_k increase exponentially with index k. Let n_s denote the number of steps per order of magnitude, then

$$c_k = c_L \cdot 10^{k/n_s} \quad \Rightarrow \quad (15)$$

$$\Delta c_k = c_{k+1} - c_k = c_L \cdot 10^{(k+1)/n_s} - c_L \cdot 10^{k/n_s} = c_L \cdot 10^{k/n_s} \cdot \left(10^{1/n_s} - 1\right), \quad (16)$$

so that

$$\frac{\Delta c_k}{c_k} = \frac{c_L \cdot 10^{k/n_s} \cdot \left(10^{1/n_s} - 1\right)}{c_L \cdot 10^{k/n_s}} = 10^{1/n_s} - 1 = const. \quad (17)$$

The final expression for the joint probability distribution therefore becomes

$$p\left(m_1, m_2 \mid D\right) \propto \sum_{k=0}^{k_H} \left[\sum_{i=1}^{n} \left(U^*_i - c_L \cdot 10^{k/n_s} \cdot \Pi_{2,i}^{m_1} \cdot \Pi_{3,i}^{m_2}\right)^2 \right]^{-n/2}, \quad (18)$$

with $k_H = n_s \log_{10}\left(c_H / c_L\right)$. In this form, the joint probability distribution can be computed easily with very good resolution on a standard stand-alone computer.

REFERENCES

[1]   Deardorff JW, Willis GE, Lilly DK. Laboratory investigation of non-steady penetrative convection. J Fluid Mech 1969; 35: 7-31.
[2]   Willis GE, Deardorff JW. Laboratory model of the unstable planetary boundary layer. J Atmos Sci 1974; 31: 1297-307.
[3]   Willis GE, Deardorff JW. Laboratory simulation of the convective planetary boundary layer. Atmos Technol 1975; 7: 80-6.
[4]   Heidt FD. The growth of the mixed layer in a stratified fluid due to penetrative convection. Bound-Layer Meteor 1977; 12: 439-61.
[5]   Deardorff JW, Willis GE, Stockton BH. Laboratory studies of the entrainment zone of a convectively mixed layer. J Fluid Mech 1980; 100: 41-64.
[6]   Deardorff JW, Willis GE. Further results from a laboratory model of the convective planetary boundary layer. Bound-Layer Meteor 1985; 32: 205-36.
[7]   Deardorff JW, Willis GE. Computer and laboratory modeling of the vertical diffusion of nonbuoyant particles in the mixed layer. Adv Geophys 1974; 18B: 187-200.
[8]   Deardorff JW, Willis GE. Ground-level concentrations due to fumigation into an entraining mixed layer. Atmos Environ 1982; 16: 1159-70.
[9]   Willis GE, Deardorff JW. On the use of Taylor's translation hypothesis for diffusion in the mixed layer. Q J R Meteor Soc 1976; 102: 817-22.
[10]   Willis GE, Deardorff JW. Laboratory study of dispersion from an elevated source within a modelled convective planetary boundary layer. Atmos Environ 1978; 12: 1305-11.
[11]   Willis GE, Deardorff JW. Laboratory study of dispersion from a source in the middle of the convectively mixed layer. Atmos Environ 1981; 15: 109-17.
[12]   Willis GE, Deardorff JW. On plume rise within a convective boundary layer. Atmos Environ 1983; 17: 2435-47.
[13]   Deardorff JW. Laboratory experiments on diffusion: The use of convective mixed-layer scaling. J Clim Appl Meteor 1985; 24(11): 1143-51.
[14]   Ohba R, Kakishima S, Ito S. Water tank experiment of gas diffusion from a stack in stably and unstably stratified layers under calm conditions. Atmos Environ 1991; 25: 2063-76.
[15]   Hibberd MF, Sawford BL, Design criteria for water tank models of dispersion in the planetary convective boundary layer. Bound-Layer Meteor 1994; 67: 97-118.
[16]   Hibberd MF, Sawford BL. A saline laboratory model of the planetary convective boundary layer. Bound-Layer Meteor 1994; 67: 229-50.
[17]   Luhar AK, Hibberd MF, Hurley PJ. Comparison of closure schemes used to specify the velocity PDF in Lagrangian stochastic dispersion models for convective conditions. Atmos Environ 1996; 30: 1407-18.
[18]   Park OH, Seo SJ, Lee SH. Laboratory simulation of vertical plume dispersion within a convective boundary layer. Bound-Layer Meteor 2001; 99: 159-69.
[19]   Snyder WH, Lawson RE Jr, Shipman MS, Lu J. Fluid modelling of atmospheric dispersion in the convective boundary layer. Bound-Layer Meteor 2002; 102: 335-66.
[20]   van Dop H, van As D, van Herwijnen A, Hibberd MF, Jonker H. Length scales of scalar diffusion in the convective boundary layer: laboratory observations. Bound-Layer Meteor 2005; 116: 1-35.
[21]   Mitsumoto S, Ueda H, Ozoe H. A laboratory experiment on the dynamics of the land and sea breeze. J Atmos Sci 1983; 40: 1228-40.
[22]   Lu J, Arya SP, Snyder WH, Lawson RE Jr. A laboratory study of the urban heat island in a calm and stably stratified environment. Part I: Temperature field. J Appl Meteor 1997; 36: 1377-91.
[23]   Lu J, Arya SP, Snyder WH, Lawson RE Jr. A laboratory study of the urban heat island in a calm and stably stratified environment. Part II: Velocity field. J Appl Meteor 1997; 36: 1392-402.
[24]   Cenedese A, Monti P. Interaction between an inland urban heat island and a sea-breeze flow: A laboratory study. J Appl Meteor 2003; 42: 1569-83.
[25]   Mitsumoto S. A laboratory experiment on the slope wind. J Meteor Soc Japan 1989; 67: 565-74.
[26]   Chen RR, Berman NS, Boyer DL, Fernando HJS. Physical model of diurnal heating in the vicinity of a two-dimensional ridge. J Atmos Sci 1996; 53: 62-85.
[27]   Hunt JCR, Fernando HJS, Princevac M. Unsteady thermally driven flows on gentle slopes. J Atmos Sci 2003; 60: 2169-82.
[28]   Deardorff JW, Willis GE. Turbulence within a baroclinic laboratory mixed layer above a sloping surface. J Atmos Sci 1987; 44: 772-78.
[29]   Reuten C, Steyn DG, Allen SE. Water-Tank studies of atmospheric boundary layer structure and air-pollution transport in upslope flow systems. J Geophys Res 2007; 112: D11114.
[30]   Reuten C, Steyn DG, Strawbridge KB, Bovis P. Observations of the relation between upslope flows and the convective boundary layer in steep terrain. Bound-Layer Meteor 2005; 116: 37-61.
[31]   Garratt JR. The atmospheric boundary layer. 1st paperback ed. Cambridge Univ Press: Cambridge, UK 1994.
[32]   Buckingham E. On physically similar systems; illustrations of the use of dimensional equations. Phys Rev Lett 1914; Second Series, IV: 345-376.
[33]   Lilly DK. Models of cloud-topped mixed layers under a strong inversion. Q J R Meteor Soc 1968; 94: 292-309.
[34]   Carson DJ. The development of a dry inversion-capped convectively unstable boundary layer. Q J R Meteor Soc 1973; 99: 450-67.
[35]   Plate, EJ. Convective boundary layer: a historical introduction. In: Buoyant Convection in Geophysical Flows. Plate EJ, *et al.*, Eds. Kluwer Acad Pub 1998: 1-22.
[36]   Schumann U. Large-eddy simulation of the upslope boundary layer. Q J R Meteor Soc 1990; 116: 637-70.
[37]   Simpson JE. Gravity currents in the environment and the laboratory. 2nd ed, Cambridge Univ Press: Cambridge, UK 1997.
[38]   Britter RE, Linden PF. The motion of the front of a gravity current traveling down an incline. J Fluid Mech 1980; 99: 531-43.
[39]   Reuten C. "Scaling and kinematics of daytime slope flow systems," The University of British Columbia, Vancouver, Canada, 2006.

[40]   Obasaju ED, Robins AG. Simulation of pollution dispersion using small scale physical models – An assessment of scaling options. Bound-Layer Meteor 1998; 52: 239-54.

[41]   Schlichting H. Boundary-layer theory. 7th ed, McGraw-Hill: Hamburg, Germany 1979.

[42]   Hinze JO. Turbulence: An introduction to its mechanism and theory. 2nd ed, McGraw-Hill: New York, USA 1975.

[43]   Stull R. A convective transport theory for surface fluxes. J Atmos Sci 1994; 51: 3-22.

[44]   Santoso E, Stull R. Convective transport theory: Further evaluation, and evidence of counter-difference surface heat fluxes. Boundary Layer Research Team Tech. Rep. BLRT-98-3, 1998. (Available from rstull@eos.ubc.ca)

[45]   Greischar L, Stull R. Convective transport theory for surface fluxes tested over the western pacific warm pool. J Atmos Sci 1999; 56: 2201-11.

[46]   Brutsaert W. Evaporation into the atmosphere. Kluwer: Dordrecht, The Netherlands 1982.

[47]   Sivia DS. Data analysis. A Bayesian tutorial. Oxford University Press: Oxford, UK 1996.

[48]   Jaynes ET. Probability theory. The logic of science. Cambridge Univ Press, Cambridge, USA 2003.

[49]   Gelman A, Carlin JB, Stern HS, Rubin DB. Bayesian data analysis. 2nd ed, Chapman & Hall/CRC: Boca Raton, USA 2004.

[50]   Gregory P. Bayesian logical data analysis for the physical sciences. Cambridge Univ Press, Cambridge, UK 2005.